Nanoscale

PAPER

View Article Online
View Journal | View Issue

Cite this: *Nanoscale*, 2024, **16**, 12992

Electron repulsion tuned electronic structure of TiO_2 by fluorination for efficient and selective photocatalytic ammonia generation†

Huiling Zhu, Xiangran Xu, Yongchao Wang, Jian Ding, Xinru Yu, Xiaoyi Liu, Zhaowu Zeng, Huan Wang, Zhen Li and Yang Wang *

Received 25th April 2024,
Accepted 11th June 2024

DOI: 10.1039/d4nr01787k

rsc.li/nanoscale

The photocatalytic conversion of nitrogen into high-value ammonia products holds tremendous potential in the global nitrogen cycle. However, the activation of N_2 and competition of hydrogen evolution limit the improvement of nitrogen fixation performance. In this study, we developed a fluorinated TiO_2 (F-TiO_2) using a hydrothermal-annealing method. The incorporation of F dopants not only enhances the adsorption and activation of N_2 through electronic structure regulation, but also facilitates an *in situ* increase in active sites *via* the electron repulsion effect between F and Ti atoms. In addition, the presence of F on the surface effectively improved the nitrogen supply problem and optimized the nitrogen fixation selectivity for its hydrophobic modulation. The NH_3 yield of the F-TiO_2 photocatalyst reached 63.8 μmol h^{-1} g^{-1}, which was 8.5 times higher than that of pure TiO_2. And the selectivity experiment showed that the electronic ratio of NH_3 to H_2 production reached 0.890. This research offers valuable insights for the design of highly efficient and selective nitrogen-fixing photocatalysts.

1. Introduction

Ammonia (NH_3), which is critical for sustained human survival, is an essential ingredient for agriculture and industry. The Haber–Bosch process continues to be the dominant industrial method for ammonia production.[1–5] However, its stringent processing conditions (400–500 °C, 150–250 atm) demand substantial energy input and result in significant carbon emissions, accounting for 1.8% of the worldwide total carbon dioxide emissions.[6,7] At present, the photocatalytic nitrogen fixation technology powered by solar energy, using nitrogen and water as the sources, with low energy consumption and mild conditions has attracted in-depth research.[8–10]

The photocatalytic nitrogen reduction reaction (NRR) offers an environmentally sustainable alternative to the Haber–Bosch process currently used in industry. However, this process is still limited by N_2 activation and the competitive hydrogen evolution reaction (HER).[11,12] As a prerequisite for the NRR, N_2 activation is difficult to achieve under mild conditions because of its large HOMO ($2\sigma_g$)–LUMO ($1\pi_u$) energy gap and the large bond energy.[13,14] Developing highly efficient active sites in photocatalysts is a key means to achieve efficient nitrogen reduction. Numerous studies have shown that the low valence metal centers of transition metal oxides can serve as active sites for inducing localized electron reduction of N_2.[15] Recently, Hirakawa *et al.* found that Ti^{3+} species in TiO_2 can provide electrons for the anti-bonding π^* orbitals of N_2, which greatly facilitates the breaking of N≡N bonds.[16] Han *et al.* also demonstrated that the high concentration of Ti^{3+} sites in C-TiO_x is the main reason for the enhanced N_2 photoreduction activity.[17] However, the oxidation of the constructed low valence metal sites during the nitrogen fixation process and the relatively moderate degree of electron localization restrict the efficient activation of N_2, thus impeding catalytic performance.[18] From this, doping-induced local electronic structure regulation was used to improve the catalytically active sites for nitrogen fixation.[19–22] The process of dopant reconfiguration of active sites during formation, however, remains unclear at this stage.

The competition with hydrogen evolution limits the selectivity, also posing a significant challenge to photocatalytic nitrogen fixation. In the photocatalytic nitrogen fixation reaction, the gas–solid–liquid three-phase interface composed of N_2, the photocatalyst and aqueous solution has abundant nitrogen and proton supply, which is an ideal interface for the nitrogen fixation reaction.[23–26] However, the extremely low solubility in water, poor adsorption and poor transport efficiency of N_2 limit its supply.[27,28] The scarcity of nitrogen results in the exacerbation of the side reaction involving hydrogen evolution.

Faculty of Materials Science and Chemistry, China University of Geosciences, Wuhan, 430074, PR China. E-mail: wyisian@cug.edu.cn

† Electronic supplementary information (ESI) available. See DOI: https://doi.org/10.1039/d4nr01787k

By means of hydrophobic modification, an efficient three-phase interface is constructed to establish a transmission channel for nitrogen to the catalyst interface, which proves to be an effective approach in addressing the issue of nitrogen supply.[29,30] Recently, Jang used oxygen-vacant TiO_2 photocatalysts embedded in poly(*N*-isopropyl acrylamide) and enhanced the nitrogen fixation capability through the addition of nitrogen in the three-phase system.[31] Sun *et al.* constructed a TiO_2-based three-phase contact system, which overcame the mass transfer limitations of N_2.[32]

In this study, we synthesized fluorinated TiO_2 (F-TiO_2) to achieve photocatalytic nitrogen reduction under the ambient atmosphere. The introduction of F modulates the electronic structure and enhances the nitrogen activation, and facilitates the generation of a large number of Ti^{3+} active sites *in situ* for efficient photocatalytic nitrogen fixation. In addition, the three-phase interface formed by the surface fluorine effectively improved the nitrogen fixation selectivity. Therefore, under the synergistic effects of the fluoride-built active sites and the three phase interface, the catalyst exhibited excellent nitrogen fixation performance.

2. Experimental section

2.1 Chemicals

Tetrabutyl titanate ($Ti(OBu)_4$) was purchased from Aladdin and hydrofluoric acid (HF, 40%) was purchased from Sinopharm Chemical Reagent Co., Ltd, and both were used without further purification. Deionized water was used in all experiments.

2.1 Catalyst synthesis

The fluorinated TiO_2 nanosheets (F-TiO_2) were synthesized by a typical solvothermal-annealing method. First, 10 mL of tetrabutyl titanate and a certain amount of hydrofluoric acid with 40% mass concentration were mixed and stirred for 30 min, and the mixture was poured into a 50 mL polytetrafluoroethylene-lined autoclave and kept at 180 °C for 24 h. The precipitate was collected by centrifugation (8000 rpm, 10 min), washed with deionized water three times, and dried at 80 °C for 12 h. The samples were labeled as s-F-TiO_2. Finally, the fluorinated TiO_2 nanosheets were prepared by calcination at 200 °C in a hydrogen atmosphere (9% Ar/H_2 gas mixture) with a flow rate of 100 mL min^{-1} for 2 h. On the basis of the experimental conditions, the samples were named *x*f-TiO_2 (*x* indicates different HF additions). In addition, the TiO_2 nanosheets without F were obtained by calcining s-F-TiO_2 at 550 °C for 2 h under environmental conditions.

3. Results and discussion

TiO_2 nanosheets with surface fluorination (s-F-TiO_2) were synthesized by using the typical hydrothermal method, as detailed in the experimental section. Subsequently, annealing was conducted in an Ar/H_2 atmosphere to achieve subsurface fluorine-doped TiO_2 (F-TiO_2), as depicted in Fig. 1a. In order to visually characterize the morphology and structural information of the fluorinated titanium dioxide nanosheets, SEM and TEM observations were conducted. SEM images (Fig. 1b and c) show that both s-F-TiO_2 and F-TiO_2 have the same nanosheet structure, indicating that atmospheric annealing does not destroy the nanostructure of the sample. As shown in Fig. 1d, it is evident that the F-TiO_2 sample appears semi-transparent under the electron beam, indicating its thin thickness. Furthermore, the HRTEM images of F-TiO_2 in Fig. 1e and f display the (001) and (100) crystal planes of anatase TiO_2, with interplanar spacings of 2.3 Å and 1.9 Å, respectively. The mapping image in Fig. 1g shows that the major elements Ti, O and F are uniformly distributed throughout the region, indicating successful and stable doping of fluorine (Fig. S1†). And the actual doping amount of F in 1.2F-TiO_2 was determined to be 5.64 at% (Table S1†).

Fig. 2a clearly reveals that the XRD diffraction patterns of all the samples consistently show the characteristic peaks of anatase titanium dioxide, indicating that fluorination does not affect the phase structure. It should be noted that the peak intensity gradually decreases with the increase of HF. This is due to the etching effect of F ions, resulting in a gradual decrease in the grain size of the nanosheets, as shown in Fig. S2.† Raman tests were performed to determine the surface structure, as shown in Fig. 2b. The four peaks at 145, 394, 517 and 636 cm^{-1} are attributed to the vibrational modes of the E_g, E_{1g}, A_{1g} and E_g peaks of anatase-phase titanium dioxide, respectively.[33] Obviously, the peak intensities also decreased with the increasing HF, which is consistent with the results of XRD.

The surface chemical states of F-TiO_2 were determined by XPS. The survey spectra show that F-TiO_2 contains only F, Ti, and O with the chemical binding energies of F 1s (684.7 eV), Ti 2p (458.5 eV), and O 1s (530.8 eV), respectively (Fig. S3†), suggesting the high purity of the as-synthesized F-TiO_2. The Ti 2p XPS spectra of s-F-TiO_2 and F-TiO_2 are shown in Fig. 2c. Compared with s-F-TiO_2, the Ti 2p3/2 peak of F-TiO_2 shifted from 458.5 eV to a lower binding energy, owing to an electron density increase on the Ti atom in TiO_2, revealing the doping of F during annealing. Additionally, two new binding energy peaks at 461.3 eV and 456.7 eV are observed, which may correspond to the Ti^{3+} in F-TiO_2. Fig. 2d shows the binding energies of F 1s in s-F-TiO_2 and F-TiO_2. Consistent with Ti 2p, the position of the peak is shifted to the right after fluorination, which reflects the increase in electron density due to the dense row of charges excited by Ti–F repulsion.[34] This is consistent with the differential charge distribution in the model of F-TiO_2 (Fig. S4†). In terms of s-F-TiO_2, the peak located at 684.5 eV corresponds to the surface Ti–F, which may be due to the substitution of the surface hydroxyl groups by F.[35] In fact, this structure can capture photo-generated electrons and facilitate the separation of photo-generated charges, thus enhancing the separation of photo-generated carriers.[36] Furthermore, the adhesion of F on the surface will form strong polar bonds at

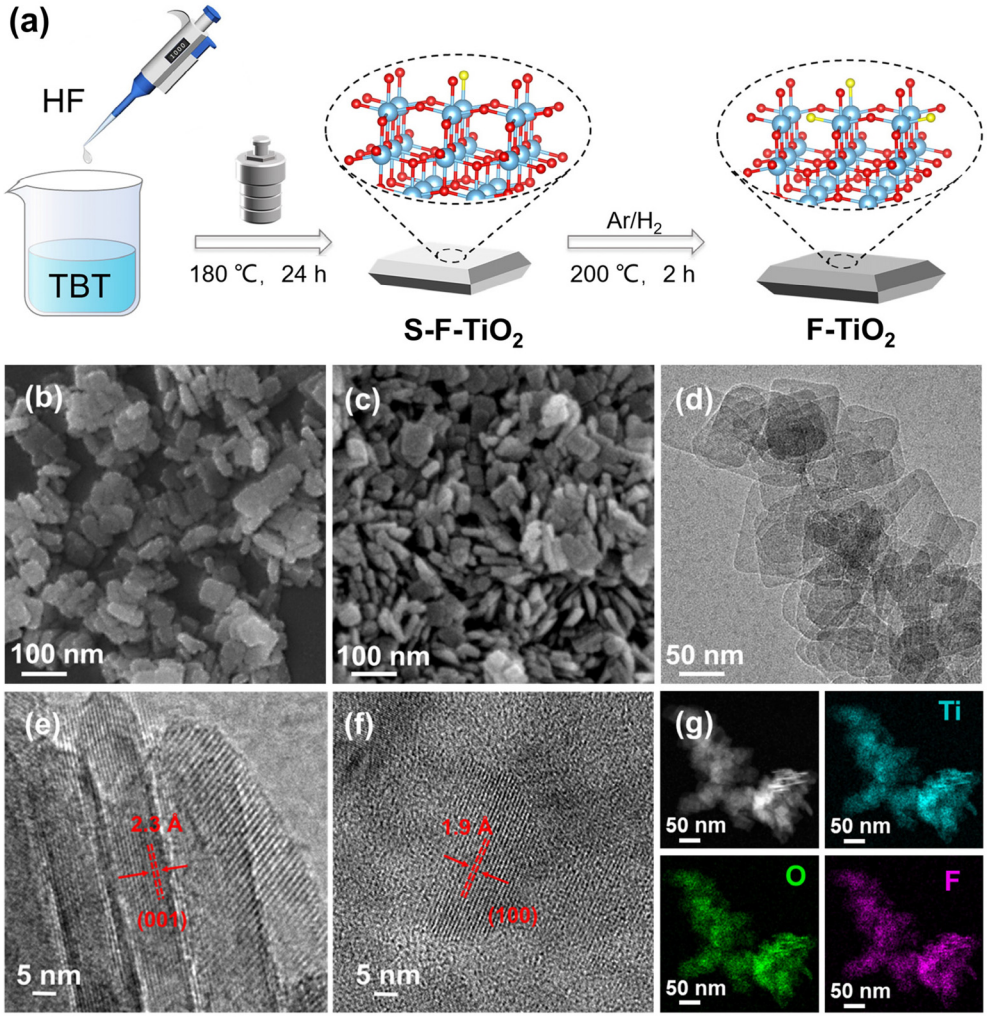

Fig. 1 (a) Illustration of the synthetic process for F-TiO_2. SEM images of (b) s-F-TiO_2 and (c) F-TiO_2. (d) TEM, (e and f) HRTEM and (g) element mapping images of F-TiO_2.

the interface, which will improve the surface hydrophobicity of titanium dioxide.[37] Notably, a new peak at 686.1 eV appears in F-TiO_2, indicating that the surface Ti–F bonds of s-F-TiO_2 partially reconfigured into sub-surface Ti–F–Ti bonds. This is consistent with the FT-IR results (Fig. S5†). The formation of Ti–F–Ti will further induce electron repulsion effects.[38] Fig. 2e shows the O 1s spectra of s-F-TiO_2 and F-TiO_2. The peaks at 529.8 eV, 531.0 eV, and 532.5 eV are attributed to lattice oxygen (Ti^{4+}–O), V_O, and surface hydroxyl oxygen, respectively. It can be found that the peaks of defective oxygen vacancies are significantly enhanced after annealing. Combined with the analysis of the Ti 2p spectra in Fig. 2c, the enhancing effect of F doping on the active sites for nitrogen fixation has been elucidated. Additionally, in order to validate the presence of surface defects in the F-TiO_2 sample, electron paramagnetic resonance (EPR) experiments were conducted. As shown in Fig. 2f, the TiO_2-based samples exhibited an obvious paramagnetic resonance signal of Ti^{3+} at a g value of 1.930.[39] Notably, F-TiO_2 showed a more intense signal of Ti^{3+}, indicating that F doping played a beneficial role in the formation of active sites.

Photocatalytic nitrogen fixation experiments were conducted under simulated sunlight and ambient conditions, where N_2-saturated water was employed as the reaction precursor and methanol served as the hole-depleting agent. The photocatalytic performance of the samples for nitrogen fixation was evaluated by using the Nessler's reagent method (Fig. S6†). Photocatalytic nitrogen fixation always adheres to a strict ammonia dosing protocol (Fig. S7†) and the nitrogen gas and reaction vessel are purged prior to the nitrogen fixation reaction (Fig. S8†).[40,41] As shown in Fig. 3a, among all the samples, 1.2F-TiO_2 exhibited the optimal nitrogen fixation rate of 63.8 μmol h^{-1} g^{-1}, which is 7 and 3 times higher than the pure TiO_2 and s-1.2F-TiO_2, respectively. The efficiency of NH_3 yield by 1.2F-TiO_2 is comparable to that of previously reported advanced anatase based photocatalysts (Table S2†). Fig. 3b presents the cyclic test of NH_3 yield rate with F-TiO_2. Apparently,

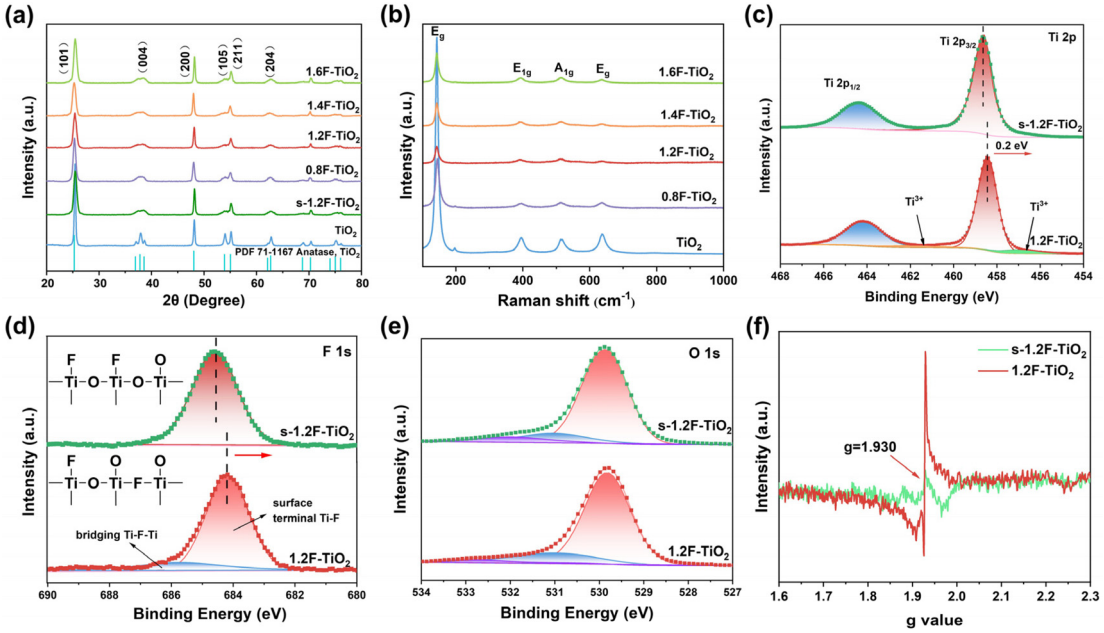

Fig. 2 (a) XRD patterns of TiO_2, s-1.2F-TiO_2 and F-TiO_2. (b) Raman spectra of TiO_2 and F-TiO_2. (c) Ti 2p, (d) F 1s, (e) O 1s XPS, and (f) EPR spectra of s-1.2F-TiO_2 and 1.2F-TiO_2.

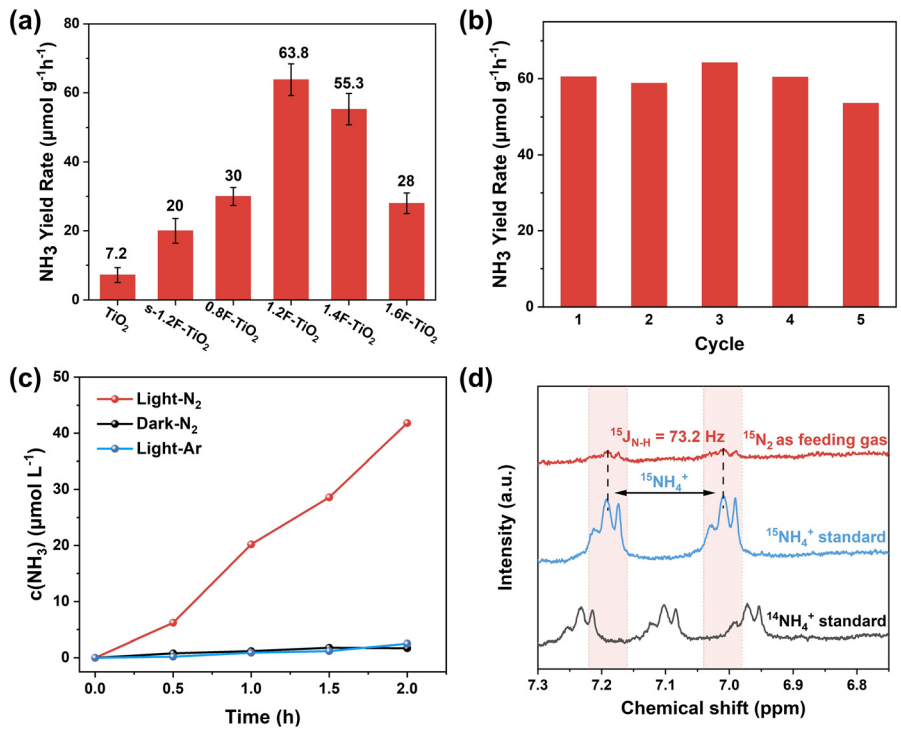

Fig. 3 (a) Photocatalytic ammonia yield rates of TiO_2, s-1.2F-TiO_2 and *x*F-TiO_2. (b) Recycling experiments of 1.2F-TiO_2. (c) NH_3 production *versus* time over 1.2F-TiO_2 with various reaction conditions. (d) The ^1H NMR spectra of 1.2F-TiO_2 bubbled with a $^{15}N_2$ atmosphere.

the ammonia yield was found to be basically unchanged after five repetitions of the photocatalytic experiments for 10 h, which suggests that F-TiO_2 has a high stability under full-spectrum light irradiation. In comparison to the remarkable NH_3 yield capability of F-TiO_2 in N_2-saturated water under irradiation, minimal NH_3 production was observed in N_2-saturated water without irradiation and in Ar-saturated water (Fig. 3c), indicating that the presence of N_2 is essential for

photocatalytic nitrogen generation. The ^{1}H NMR spectra of standard $^{15}NH_4^+$, $^{14}NH_4^+$, and the product produced over F-TiO_2 after 1 h illumination with pure $^{15}N_2$ injected as the feed gas are shown in Fig. 3d. Notably, only a doublet signal with a spacing of 73.2 Hz was observed in the reaction solution under the $^{15}N_2$ atmosphere, which is consistent with the signal obtained from the standard $^{15}NH_4^+$ solution.[42] These results provide strong evidence that the generated NH_3 indeed originates from N_2.

In order to investigate the contribution of F in enhancing the photocatalytic activity of F-TiO_2, an analysis has been conducted on the band gap structure and corresponding photoelectrochemical properties. The UV-vis spectra of TiO_2, s-1.2F-TiO_2 and 1.2F-TiO_2 are illustrated in Fig. S9.† It was found that the fluorination could effectively improve light absorption. As shown in Fig. 4a, fluorination induced a significant reduction of the energy band gap, with E_g values of 3.14 eV and 3.22 eV for TiO_2 and F-TiO_2, respectively. Meanwhile, the positions of the valence bands can be obtained based on the tangent values of the XPS valence band edge spectra, as shown in Fig. 4b.

The electronic structure of F-TiO_2 was investigated through density functional theory (DFT) studies to gain a deeper understanding of the impact of F. As shown in Fig. 4c, the Ti 3d and O 2p orbitals predominantly form the conduction band (CB) and valence band (VB), respectively. Upon fluorination, the Fermi energy level enters the CB and gives rise to a defect band. This phenomenon can be attributed to the localized electron enrichment induced by the strong electron repulsion between F and Ti.[43–45] Obviously, the fluorine-regulated electronic structure will promote the activation of N_2.[38] In addition, the density of states (DOS) calculations show the reduction of the energy band gap and the overall downward shift of the energy band positions (Fig. S10† and Fig. 4d), which is consistent with the experimental results. As shown in Fig. 4e, we also investigated the effect of fluorination on the dynamics of photogenerated electrons in F-TiO_2 using steady-state photoluminescence (PL) spectroscopy. Compared with s-F-TiO_2, F-TiO_2 shows the lowest PL intensity, indicating the highest efficiency of charge separation. This observation is consistent with the lowest charge transfer resistance of F-TiO_2, as depicted in Fig. 4f. This finding is further confirmed by other photoelectrochemical tests (Fig. S11†).

The enhancement mechanism of the interaction between the photocatalysts and N_2 molecules was investigated using N_2 temperature-programmed desorption (TPD). Fig. 5a shows the N_2-TPD curves of TiO_2, s-1.2F-TiO_2 and 1.2F-TiO_2. The peak observed prior to reaching 300 °C was attributed to physisorption, whereas the subsequent peak following the surpassing of 350 °C originated from nitrogen chemisorption. In comparison to TiO_2 and s-1.2F-TiO_2, F-TiO_2 exhibited a significantly elevated peak, strongly indicating that the introduction of fluorine in F-TiO_2 resulted in an increased number of active sites (Ti^{3+}) and optimized electronic structure for N_2 adsorption. To gain deeper insights into the underlying mechanism behind the augmented N_2 photofixation activity, we conducted a comparative analysis of photocurrents in both inert (Ar) and active (N_2) atmospheres (Fig. S12†). The photocurrent response of TiO_2 in an Ar environment was found to be weak, as depicted in Fig. 5b. In contrast, F-TiO_2 shows a stronger photocurrent, suggesting that fluorine doping promotes charge transfer and separation effects.[46] More notably, the photocurrent of F-TiO_2

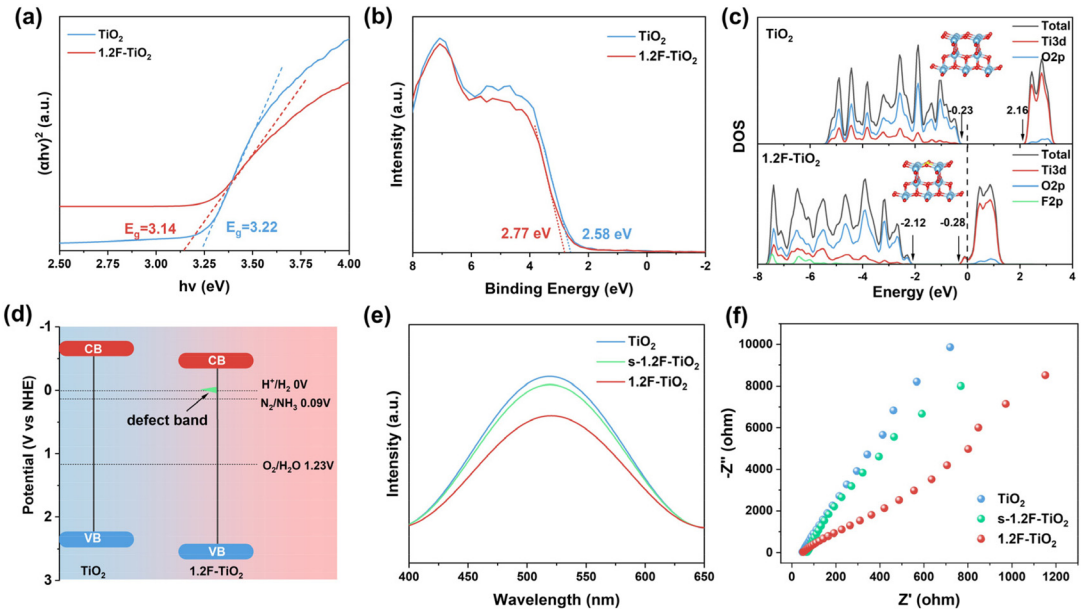

Fig. 4 (a) Optical energy band gap and (b) XPS valence band edge spectra of TiO_2 and 1.2F-TiO_2. (c) The partial wave DOS of TiO_2 and F-TiO_2. The insets are the corresponding optimized configurations of TiO_2 and F-TiO_2. (d) Schematic illustration of the energy band structures of TiO_2 and F-TiO_2. (e) Photoluminescence spectra and (f) Nyquist plots of TiO_2, s-1.2F-TiO_2 and 1.2F-TiO_2.

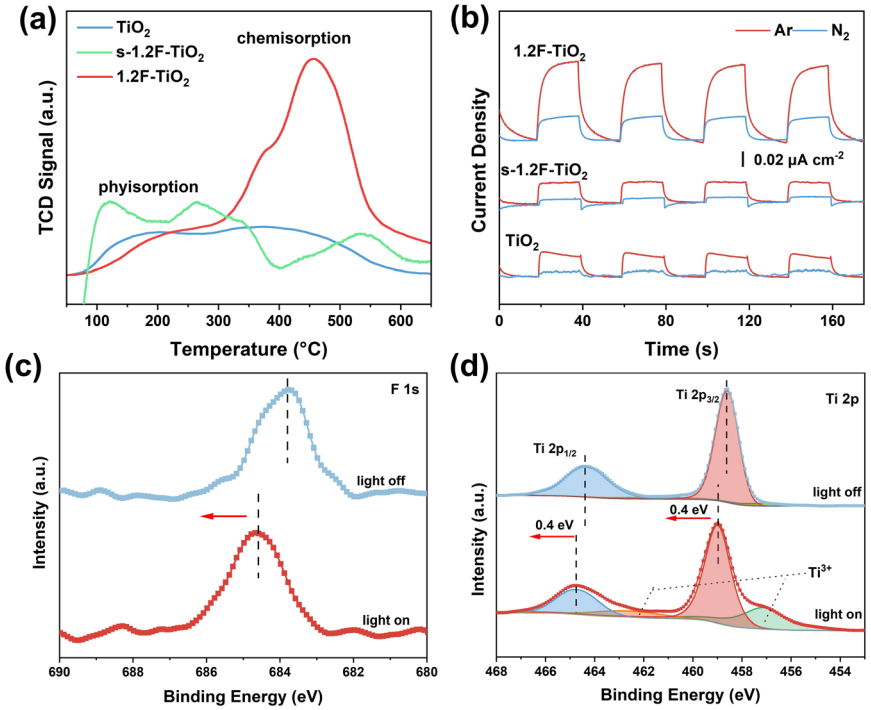

Fig. 5 (a) N_2-TPD profiles and (b) transient photocurrent curves of TiO_2, s-1.2F-TiO_2 and 1.2F-TiO_2. High-resolution XPS spectra of (c) F 1s and (d) Ti 2p in 1.2F-TiO_2 under 365 nm LED irradiation.

decreased more than that of TiO_2 when the Ar environment was changed to a nitrogen environment. The above findings suggest that fluorinated titanium dioxide possesses the capability to transfer electrons to adsorbed N_2 molecules, thereby facilitating subsequent nitrogen activation reactions.[20]

To reveal the electron interaction between F and Ti atoms, *in situ* irradiated X-ray photoelectron spectroscopy (XPS) was carried out. As shown in Fig. 5c and d, the redshifted peaks of F and Ti after illumination indicate electron loss of both F and Ti atoms.[47] The simultaneous loss of electrons from F and Ti suggests the presence of electron repulsion between them. Besides, two peaks assigned to Ti^{3+} (462.1 eV and 457.1 eV) increased dramatically.[48] This suggests that under light conditions, Ti and F undergo electron repulsion and more Ti^{3+} nitrogen-fixing active sites are generated *in situ*.[17] In addition, there is no significant change in the *in situ* irradiated XPS of s-1.2F-TiO_2 (Fig. S13†), which is more indicative of the successful internal doping of F in F-TiO_2. Due to the higher electronegativity of F, it enhances the electron-attracting ability of surface Ti–F to synergize with subsurface Ti^{3+}. This inhibits the recombination of photogenerated charge carriers on the one hand, and effectively combines with nitrogen fixation

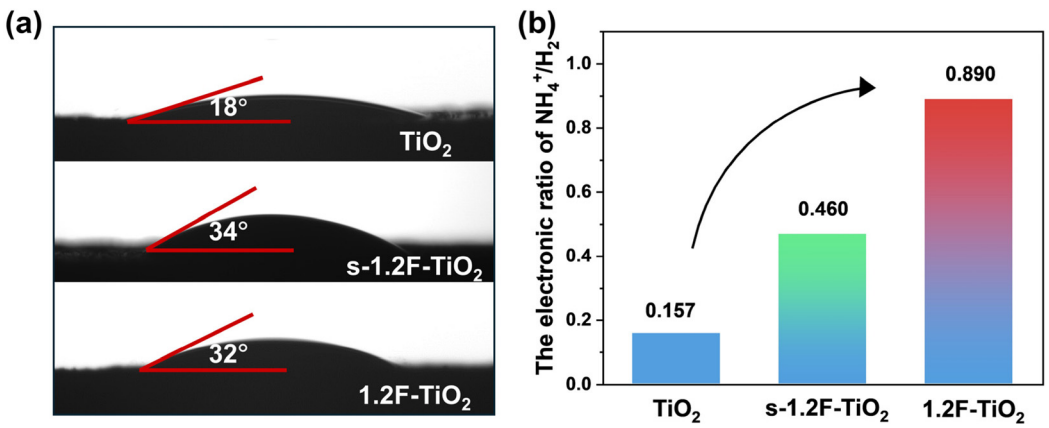

Fig. 6 (a) Contact angle measurements for TiO_2, s-1.2F-TiO_2 and 1.2F-TiO_2. (b) Photocatalytic ammonia and hydrogen production charge distribution ratio.

selectivity to facilitate photocatalytic nitrogen reduction on the other hand. The experimental results show that after the annealing treatment, F^- exists mainly in the form of fluorine bridging bonds (Ti–F–Ti) on the surface of F-TiO_2.

The surface aerophilic properties were evaluated by conducting contact angle measurements. The contact angle (Fig. 6a) changed from 18° to 32° after F modification, indicating enhanced hydrophobicity of the F-TiO_2 sample. This increase in contact angle can be attributed to the presence of a fluorine capping layer on the surface.[49] In other words, by replacing surface –OH with fluorine, hydrophilic conditions are avoided, and the van der Waals forces at the sample–water interface are strengthened, which is advantageous for the adsorption of N_2.[50,51] In addition, the hydrophobic properties also maintain good stability in the process of photocatalytic nitrogen fixation (Fig. S14†). In order to investigate the effect of hydrophobicity induced by the F-modified surfaces on nitrogen fixation selectivity, the nitrogen fixation/hydrogen production electron transfer ratio was tested. As shown in Fig. 6b, the TiO_2 nitrogen fixation to hydrogen production charge transfer ratio was tested and calculated to be 0.157, and the F-TiO_2 ratio was dramatically increased by a factor of 5 (0.890). This indicated that the hydrophobic property induced by surface fluoridation can effectively improve the selectivity of the nitrogen fixation reaction.

4. Conclusions

In conclusion, fluorinated titanium dioxide (F-TiO_2) was successfully synthesized by a hydrothermal-annealing method in this study. The catalytic activity and selectivity of nitrogen fixation were enhanced through the incorporation of F atoms, which effectively regulated the active sites and surface hydrophilicity. In view of the above, the nitrogen fixation rate of the F-TiO_2 photocatalyst reached 63.8 μmol h^{-1} g^{-1}, which was 8.5 times higher than that of TiO_2, and the electron transfer ratio of generated NH_3 to H_2 reached 0.890. This study presents a straightforward approach for the development of nitrogen-fixing photocatalysts in terms of selectivity and activity.

Data availability

The authors confirm that the data supporting the findings of this study are available within the article and its ESI.†

Conflicts of interest

The authors declare no conflict of interest.

Acknowledgements

This work was financially supported by the National Natural Science Foundation of china (52002361), the Natural Science Foundation of Hubei Province of China (No. 2020CFB267), and the Fundamental Research Funds for the Central Universities (G1323520268). The calculations were performed by using the high performance computing center for China University of Geosciences (Wuhan).

References

1 H. P. Jia and E. A. Quadrelli, *Chem. Soc. Rev.*, 2014, **43**, 547–564.
2 M. Lashgari and P. Zeinalkhani, *Appl. Catal., A*, 2017, **529**, 91–97.
3 H. K. Lee, C. S. L. Koh, Y. H. Lee, C. Liu, I. Y. Phang, X. Han, C.-K. Tsung and X. Y. Ling, *Sci. Adv.*, 2018, **4**, eaar3208.
4 M.-A. Légaré, G. Bélanger-Chabot, R. D. Dewhurst, E. Welz, I. Krummenacher, B. Engels and H. Braunschweig, *Science*, 2018, **359**, 896–900.
5 J. G. Chen, R. M. Crooks, L. C. Seefeldt, K. L. Bren, R. M. Bullock, M. Y. Darensbourg, P. L. Holland, B. Hoffman, M. J. Janik, A. K. Jones, M. G. Kanatzidis, P. King, K. M. Lancaster, S. V. Lymar, P. Pfromm, W. F. Schneider and R. R. Schrock, *Science*, 2018, **360**, eaar6611.
6 B. Yu, J. Duan, H. Cong, W. Xie, R. Liu, X. Zhuang, H. Wang, B. Qi, M. Xu, Z. L. Wang and J. Zhou, *Science*, 2020, **370**, 342–346.
7 T. Oshikiri, K. Ueno and H. Misawa, *Angew. Chem., Int. Ed.*, 2016, **55**, 3942–3946.
8 Y. Ashida, Y. Onozuka, K. Arashiba, A. Konomi, H. Tanaka, S. Kuriyama, Y. Yamazaki, K. Yoshizawa and Y. Nishibayashi, *Nat. Commun.*, 2022, **13**, 7263.
9 C. Hu, X. Chen, J. Jin, Y. Han, S. Chen, H. Ju, J. Cai, Y. Qiu, C. Gao, C. Wang, Z. Qi, R. Long, L. Song, Z. Liu and Y. Xiong, *J. Am. Chem. Soc.*, 2019, **141**, 7807–7814.
10 G. Ren, J. Zhao, Z. Zhao, Z. Li, L. Wang, Z. Zhang, C. Li and X. Meng, *Angew. Chem., Int. Ed.*, 2024, **63**, e202314408.
11 J. Chen, Y. Kang, W. Zhang, Z. Zhang, Y. Chen, Y. Yang, L. Duan, Y. Li and W. Li, *Angew. Chem., Int. Ed.*, 2022, **61**, e202203022.
12 C. Ling, Y. Zhang, Q. Li, X. Bai, L. Shi and J. Wang, *J. Am. Chem. Soc.*, 2019, **141**, 18264–18270.
13 Q. Zhuo, J. Yang, Z. Mo, X. Zhou, T. Shima, Y. Luo and Z. Hou, *J. Am. Chem. Soc.*, 2022, **144**, 6972–6980.
14 H. Li, J. Wang, Z. Ruan, P. Nan, B. Ge, M. Cheng, L. Yang, X. Li, Q. Liu, B. Pan, Q. Zhang, C. Xiao and Y. Xie, *Mater. Horiz.*, 2023, **10**, 5053–5059.
15 S. Wang, B. Ge, Z. Yang, H. Zhang, Q. Yang, C. Hu, X. Bao and P. Yuan, *ACS Catal.*, 2024, **14**, 1432–1442.
16 H. Hirakawa, M. Hashimoto, Y. Shiraishi and T. Hirai, *J. Am. Chem. Soc.*, 2017, **139**, 10929–10936.
17 Q. Han, C. Wu, H. Jiao, R. Xu, Y. Wang, J. Xie, Q. Guo and J. Tang, *Adv. Mater.*, 2021, **33**, 2008180.
18 N. Zhang, X. Feng, D. Rao, X. Deng, L. Cai, B. Qiu, R. Long, Y. Xiong, Y. Lu and Y. Chai, *Nat. Commun.*, 2020, **11**, 4066.

19 Y. Chen, M. Yu, G. Huang, Q. Chen and J. Bi, *Small*, 2022, **18**, 2205388.
20 Y. Bo, H. Wang, Y. Lin, T. Yang, R. Ye, Y. Li, C. Hu, P. Du, Y. Hu, Z. Liu, R. Long, C. Gao, B. Ye, L. Song, X. Wu and Y. Xiong, *Angew. Chem., Int. Ed.*, 2021, **60**, 16085–16092.
21 B. Chang, Z. Cao, Y. Ren, C. Chen, L. Cavallo, F. Raziq, S. Zuo, W. Zhou, Y. Han and H. Zhang, *ACS Nano*, 2024, **18**, 288–298.
22 Y. Ohki, K. Munakata, Y. Matsuoka, R. Hara, M. Kachi, K. Uchida, M. Tada, R. E. Cramer, W. M. C. Sameera, T. Takayama, Y. Sakai, S. Kuriyama, Y. Nishibayashi and K. Tanifuji, *Nature*, 2022, **607**, 86–90.
23 X. Wang, B. Wang, S. Yin, M. Xu, L. Yang and H. Sun, *J. Cleaner Prod.*, 2022, **360**, 132162.
24 G. Ren, M. Zhou, P. Hu, J.-F. Chen and H. Wang, *Nat. Commun.*, 2024, **15**, 2346.
25 A. Li, Q. Cao, G. Zhou, B. V. K. J. Schmidt, W. Zhu, X. Yuan, H. Huo, J. Gong and M. Antonietti, *Angew. Chem., Int. Ed.*, 2019, **58**, 14549–14555.
26 Z. Tang, L. Xiong, X. Zhang, J. Shen, A. Sun, X. Lin and Y. Yang, *Small*, 2022, **18**, 2105217.
27 M. Wang, J. Ma, Z. Shang, L. Fu, H. Zhang, M.-B. Li and K. Lu, *J. Mater. Chem. A*, 2023, **11**, 3871–3887.
28 S. Wu, Z. Chen, W. Yue, S. Mine, T. Toyao, M. Matsuoka, X. Xi, L. Wang and J. Zhang, *ACS Catal.*, 2021, **11**, 4362–4371.
29 H. Huang, R. Shi, Z. Li, J. Zhao, C. Su and T. Zhang, *Angew. Chem., Int. Ed.*, 2022, **61**, e202200802.
30 A. Li, Q. Cao, G. Zhou, B. V. K. J. Schmidt, W. Zhu, X. Yuan, H. Huo, J. Gong and M. Antonietti, *Angew. Chem., Int. Ed.*, 2019, **58**, 14549–14555.
31 C. Lee, H. Kim and Y. J. Jang, *ACS Appl. Energy Mater.*, 2022, **5**, 11018–11024.
32 R. Guan, D. Wang, Y. Zhang, C. Liu, W. Xu, J. Wang, Z. Zhao, M. Feng, Q. Shang and Z. Sun, *Appl. Catal., B*, 2021, **282**, 119580.
33 C. Lu, Y. Ma, Y. Cao, Q. Huang and J. Wang., *Chem. Eng. J.*, 2023, **468**, 143598.
34 Q. Sun, J. Xu, F. Tao, W. Ye, C. Zhou, J. He and J. Lu, *Angew. Chem., Int. Ed.*, 2022, **61**, e202200872.
35 S.-M. Wu, I. Hwang, B. Osuagwu, J. Will, Z. Wu, B. B. Sarma, F.-F. Pu, L.-Y. Wang, Z. Badura, G. Zoppellaro, E. Spiecker and P. Schmuki, *ACS Catal.*, 2023, **13**, 33–41.
36 H. Park, J. Phys. Chem. B., 2004, **108**, 4086–4093.
37 Z.-Y. Luo, K.-X. Chen, D.-C. Mo and S.-S. Lyu, *J. Phys. Chem. C*, 2016, **120**, 11882–11888.
38 R. Fu, Z. Wu, Z. Pan, Z. Gao, Z. Li, X. Kong and L. Li, *Angew. Chem., Int. Ed.*, 2021, **60**, 11173–11179.
39 L. Bonneviot and G. L. Haller, *J. Catal.*, 1988, **113**, 96–105.
40 S. Z. Andersen, V. Čolić, S. Yang, J. A. Schwalbe, A. C. Nielander, J. M. McEnaney, K. Enemark-Rasmussen, J. G. Baker, A. R. Singh, B. A. Rohr, M. J. Statt, S. J. Blair, S. Mezzavilla, J. Kibsgaard, P. C. K. Vesborg, M. Cargnello, S. F. Bent, T. F. Jaramillo, I. E. L. Stephens, J. K. Nørskov and I. Chorkendorff, *Nature*, 2019, **570**, 504–508.
41 Y. Zhao, R. Shi, X. Bian, C. Zhou, Y. Zhao, S. Zhang, F. Wu, G. I. N. Waterhouse, L. Wu, C. Tung and T. Zhang, *Adv. Sci.*, 2019, **6**, 1802109.
42 S. Wu, C. He, L. Wang and J. Zhang, *Chem. Eng. J.*, 2022, **443**, 136425.
43 M. Xing, Y. Zhou, C. Dong, L. Cai, L. Zeng, B. Shen, L. Pan, C. Dong, Y. Chai, J. Zhang and Y. Yin, *Nano Lett.*, 2018, **18**, 3384–3390.
44 Y. Wang, Y. Zhang, X. Zhu, Y. Liu and Z. Wu, *Appl. Catal., B*, 2022, **316**, 121610.
45 J. Yang, Y. Guo, R. Jiang, F. Qin, H. Zhang, W. Lu, J. Wang and J. C. Yu, *J. Am. Chem. Soc.*, 2018, **140**, 8497–8508.
46 X. Li, X. Wu, S. Liu, Y. Li, J. Fan and K. Lv, *Chin. J. Catal.*, 2020, **41**, 1451–1467.
47 L. Wang, B. Cheng, L. Zhang and J. Yu, *Small*, 2021, **17**, 2103447.
48 Y. Sun, H. Ji, Y. Sun, G. Zhang, H. Zhou, S. Cao, S. Liu, L. Zhang, W. Li, X. Zhu and H. Pang, *Angew. Chem., Int. Ed.*, 2024, **63**, e202316973.
49 G. Song, R. Gao, Z. Zhao, Y. Zhang, H. Tan, H. Li, D. Wang, Z. Sun and M. Feng, *Appl. Catal., B*, 2022, **301**, 120809.
50 F. Pellegrino, E. Morra, L. Mino, G. Martra, M. Chiesa and V. Maurino, *J. Phys. Chem. C*, 2020, **124**, 3141–3149.
51 J. I. Brauer and G. Szulczewski, *J. Phys. Chem. B*, 2014, **118**, 14188–14195.